Catalysis Science & Technology

This article can be cited before page numbers have been issued, to do this please use: A. Nowak, P. Jamroz, M. M. Marzec, K. Sokolowski, A. Dzimitrowicz, P. Pohl, A. Bernasik and P. Cyganowski, *Catal. Sci. Technol.*, 2026, DOI: 10.1039/D6CY00150E.

ARTICLE

View Article Online
DOI: 10.1039/D6CY00150E

Received 00th January 20xx,
Accepted 00th January 20xx

DOI: 10.1039/x0xx00000x

3D-printed flow-mode atmospheric pressure glow discharge reactor for the synthesis of multi-metallic Pt-/ Pd-/ Os-/ Ru-/ Re-/ W-/ Cr-/ nanocluster catalysts

Angelika Nowak[a]*, Piotr Jamroz[a], Mateusz M. Marzec[b], Krystian Sokolowski[b], Anna Dzimitrowicz[a], Paweł Pohl[a], Andrzej Bernasik[b,c], Piotr Cyganowski[d]*

In this study, cold atmospheric pressure plasma (CAPP) was used to synthesise “electron-rich” multi-metallic nanocluster catalysts (NCs) from precursors containing Pt, Pd, Os, Ru, Re, W and Cr, with potential applications in hydrogenation reactions. To this end, direct-current atmospheric pressure glow discharge (dc-APGD) was operated in two configurations: a flowing liquid anode (FLA) and a flowing liquid cathode (FLC). The CAPP system was fabricated using stereolithography. The NCs were characterised by dynamic light scattering and electrophoretic light scattering. Catalytic activity was evaluated using the reduction of 4-nitrophenol (4-NP) to 4-aminophenol. Morphology and surface composition were examined by high-resolution transmission electron microscopy and X-ray photoelectron spectroscopy. The NCs were predominantly smaller than 1 nm forming clustered atoms. The NCs synthesised by FLA- and FLC-dc-APGD with ruthenium as the dominant metal and tungsten as the secondary metal ($Ru^{W}NCs$) exhibited zeta potentials of 32.58 ± 0.16 mV and 32.42 ± 0.46 mV, respectively, indicating good colloidal stability. $Ru^{W}NCs$ synthesised by FLA- and FLC-dc-APGD also showed the highest 4-NP reduction activity, with mass-normalised rate constants (k_{1m}^{b}) of 17.81 min^{-1} mg^{-1} and 18.09 min^{-1} mg^{-1} (75% and 81% conversion), respectively. $Os^{Pd/Cr}NCs$ synthesised by FLA-dc-APGD demonstrated comparable catalytic performance (k_{1m}^{b} = 15.87 min^{-1} mg^{-1}), achieving 86% 4-NP conversion. Notably, this conversion was attained within 1.2 min, whereas all reported values correspond to a reaction time of 8 min.

Introduction

Metal particles at the nanoscale have attracted considerable attention in recent years owing to their catalytic behaviour, which is strongly governed by their high surface-to-volume ratio [1]. The smallest nanostructures, with average sizes below 10 nm, play a particularly important role in catalytic processes, offering substantial increases in the rates of a various reactions [2,3]. Among these, structures with sizes close to or below 1 nm are of greatest interest [3,4], as transition-metal particles consisting of approximately 12–20 atoms are recognised as the most catalytically active species [4]. In this context, recent studies have demonstrated that the selected “electron-rich” d-block elements, such as Au [5,6], Pt [7], Pd [8], Ru [9,10], Ir [11], Os [9], Rh [9,12] and Re [13], exhibit a strong tendency to form exceptionally small particles, including atom nanoclusters and sub-nanoclusters. These structures represent a new generation of catalysts that may play a crucial role in key chemical processes [5,14], including catalytic hydrogenation reactions.

Among d-block metals, platinum (Pt), palladium (Pd), osmium (Os), ruthenium (Ru), rhenium (Re), tungsten (W) and chromium (Cr) are of particular significance due to their distinctive catalytic properties in hydrogenation [15–18], oxidation [19–22], ammonia synthesis [10], electrocatalytic processes [23] and polymerisation reactions [24,25]. Synthesising these metals as nanocatalysts comprising only a few to several dozen atoms offers significant opportunities to enhance catalytic activity, selectivity and durability through size-dependent effects and the increased availability of surface atoms.

Platinum- and palladium-based catalysts are widely employed in fuel cells [26,2], exhaust gas treatment [28,29] and fine chemical synthesis [30,31]; however, their conventional synthesis methods often require high temperatures, organic solvents or multi-step processes, which limit scalability and environmental sustainability. Similarly, osmium-based catalysts exhibit strong hydrogen affinity and high catalytic potential in hydrogenation and sensing applications [32], yet their synthesis is constrained by high reactivity under oxidative conditions and reliance on complex preparation routes. Ruthenium catalysts, which are essential in both homogeneous and heterogeneous systems, are typically synthesised via polyol reduction [33,34] or calcination-based method [33,35], both of which involve harsh conditions and multiple reagents. Ruthenium nanoparticles (NPs) are widely recognized as efficient catalyst for organic transformations, including Fischer-Tropsch synthesis, ammonia synthesis, oxidation and reduction processes, as well as C–C coupling reactions [36]. Rhenium NPs find applications in medicine, fuel cells, hydrogen evolution reaction, and catalysis [37], and can be prepared, for example, by pulsed-laser decomposition of NH_4ReO_4 or $Re_2(CO)_{10}$ [38], as well as through microemulsion-based synthesis routes [39]. Tungsten-based materials play a vital

---

[a] Department of Analytical Chemistry and Chemical Metallurgy, Wroclaw University of Science and Technology, Wybrzeze St. Wyspianskiego 27, 50-370 Wroclaw, Poland
[b] Academic Centre for Materials and Nanotechnology, AGH University of Krakow, A. Mickiewicza 30, 30-059 Krakow, Poland
[c] Faculty of Physics and Applied Computer Science, AGH University of Krakow, A. Mickiewicza 30, 30-059 Krakow, Poland
[d] Department of Process Engineering and Technology of Polymer and Carbon Materials, Wroclaw University of Science and Technology, Wybrzeze St. Wyspianskiego 27, 50-370 Wroclaw, Poland
*Corresponding authors: Angelika Nowak (angelika.nowak@pwr.edu.pl) and Piotr Cyganowski (piotr.cyganowski@pwr.edu.pl)

Supplementary Information available: All data associated with the synthesis and evaluation of the catalysts presented in this study are available under the permanent identifier. See DOI: https://doi.org/10.18150/SSL3GB.

DOI: 10.1039/D6CY00150E

role in energy-related applications [40]; however, precise control over sub-10 nm tungsten clusters remains limited, despite the well-established relationship between particle size, dispersion, and catalytic performance. Chromium-based catalysts are commonly prepared via incipient wetness impregnation, followed by drying and calcination to obtain highly dispersed and catalytically active chromium species, which are widely used in propane dehydrogenation [41].

Given their industrial relevance, the development of simple, scalable and user-friendly synthesis methods for multi-metallic nanocluster catalysts (NCs) derived from precursors containing Pt, Pd, Os, Ru, Re, W and Cr is both scientifically and practically important. To achieve catalysts with high activity, selectivity and long-term stability, a range of modification strategies has been explored, including surfactant-assisted [42], halogenation [43], acid-base [44,45] and chelating-agent-based approaches [46]. Nevertheless, synthesis routes for Pt-, Pd-, Os-, Ru-, Re-, W- and Cr-based catalysts typically rely on elevated temperatures and organic reagents, rendering these processes labour-intensive and cost-prohibitive [26,47]. In this context, the present study aims to develop a novel method for the synthesis of multi-metallic nanoclusters for catalytic hydrogenation reactions. To this end, a unique plasma-based system is employed, consisting of a 3D-printed continuous-flow reactor in which direct-current atmospheric pressure glow discharge (dc-APGD) is generated and operated without the need for additional discharge gases or chemical reducing agents. In this approach, aqueous solutions of metal precursors are continuously introduced into the reactor, where highly reactive species such as electrons, ions, radicals and excited atoms [48] enable the efficient formation of metallic nanocatalysts.

Waste materials containing d-block metals, such as spent catalysts, superalloys or intermediate products from mineral processing, represent a valuable resource that can be recovered and transformed into catalytically active substances. In this context, a representative mixture of secondary raw materials was simulated by selecting metals that commonly occur in key secondary sources. Pt, Pd, Os, Ru, and Re are predominantly found in spent automotive catalytic converters and other industrial catalyst residues [49–52], where their concentrations can exceed those in primary ores by orders of magnitude, making these waste streams important secondary reservoirs [49,52]. To simulate such a mixture of secondary raw materials, we investigated multi-metallic solutions containing Pt, Pd, Os, Ru, Re, with W and Cr that were treated using cold atmospheric pressure plasma (CAPP) to produce catalytically active NCs. This results from the fact that CAPP systems generate specific reactive oxygen species (ROS) and reactive nitrogen species (RNS), which possess distinct redox potentials that facilitate the reduction of metal ions to their corresponding metallic nanoscale form [53]. The application of multi-metallic NCs, in which metals with lower work functions, can donate electrons to metals with higher work functions, facilitates electron transfer and enhances the catalytic activity of the NCs. This electron transfer can adjust the electronic configuration of the active sites, further improving their catalytic performance [54]. From this perspective, the use of d-block metals that are rich in electrons and potentially recoverable from secondary raw materials is advantageous not only in terms of cost but also due to their intrinsic catalytic properties. Accordingly, the present work provides a comprehensive overview of catalysts based on d-block metal NPs that can be synthesised in a 3D-printed, flow-mode atmospheric pressure glow discharge reactor from precursor solutions derived, for example, from the processing of secondary resources.

Importantly, this study reports the first successful synthesis of osmium-based NCs using a plasma-based approach, underscoring the innovative nature of the methodology. While NPs and catalysts based on Pt, Pd, Ru, Re, W and Cr have previously been synthesised using plasma-assisted methods [53,55–60], none of these studies has explored the synthesis of multi-metallic NCs using a 3D-printed, continuous-flow CAPP system.

Complementing conventional synthesis methods, plasma-assisted techniques have attracted increasing attention due to their ability to finely control nanocatalyst characteristics. For example, glow discharge-assisted method enable the formation of monodisperse ultrafine ruthenium catalyst supported on TiO_2 [57]. Mixed tungsten and cobalt oxides-based thin films were produced by plasma-enhanced chemical vapor deposition, and this catalyst can be used for catalytic materials for CO_2 conversion [61]. Green methods for nanocatalyst synthesis are also available, encompassing immobilized gold nanoparticles synthesized by RF plasma [62], and Ag nanoparticles on N-doped TiO_2 nanotubes synthesized by atmospheric pressure dielectric barrier discharge [63]. The aforementioned plasma-assisted nanocatalyst synthesis methods rely on support compounds [57,63] and are multistep [62], thereby increasing process complexity and reagent consumption. Notably, our previous research demonstrated the synthesis of rhenium nanoparticles by pulse-modulated radio-frequency atmospheric-pressure glow discharge [64] and direct-current atmospheric pressure glow discharge (dc-APGD) [53], as well as fructose and Arabic gum stabilized rhenium nanoparticles by dc-APGD [65,66]. Furthermore, the dc-APGD was employed for the synthesis of poly(vinylpyrrolidone)-stabilized platinum nanoparticles [67] and hydrogel-based nanocomposite catalyst containing uncoated gold nanoparticles [68]. These nanocatalysts were utilized for the hydrogenation of nitroaromatic compounds [53,64,66,68], deactivation of antimicrobial agents [65], and heat management systems for internal combustion chambers [67]. The advancement presented in this work consist of plasma system with its dedicated design, developed specifically to meet the requirements of the conducted research. The applied design solution provide a high degree of modularity and facilitate rapid reconfiguration, thereby enhancing the versality and applicability of the system for CAPP-studies. Moreover, the system incorporates dedicated technological solutions, such as threaded adjustment mechanisms, which enable precise control of the electrode position and, consequently, accurate regulation of the discharge gap height.

It is anticipated that the use of a 3D-printed, flow-mode reactor will enable the efficient synthesis of d-block metal NCs.

In this study, we report the first use of a 3D-printed CAPP reactor for the synthesis of nanocatalysts comprising Pt, Os, Ru, W and Re as the dominant metals in the “electron-rich” structures particularly important for the hydrogenation reactions. Multi-metallicity was achieved through the incorporation of accompanying metals, including Os, Pd/Cr, W and Ru/Os. The adoption of stereolithography (SLA) facilitated the precise design and fabrication of a reactor tailored to the operational requirements of the experimental framework. These requirements included, among others, maximising the duration of precursor exposure to the CAPP, ensuring uniform product collection, enabling continuous precursor delivery, and allowing flexible control of electrode positioning. To identify the most efficient synthetic route for NC formation, a comparative study was conducted using flowing liquid anode direct-current atmospheric pressure glow discharge (FLA-dc-APGD) and flowing liquid cathode direct-current atmospheric pressure glow discharge (FLC-dc-APGD) configurations. This approach enabled systematic evaluation of the effects of different discharge configurations, thereby allowing the determination of optimal synthesis conditions for enhanced catalytic performance. The efficiency of NC synthesis was quantitatively assessed using a model catalytic reaction, namely the reduction of 4-nitrophenol (4-NP) catalysed by the synthesised NCs. The application of the CAPP reactor under these conditions enabled the effective production of catalytically active NCs.

Experimental section

View Article Online
DOI: 10.1039/D6CY00150E

A detailed list of reagents, instrumentation, and experimental procedures is provided in the Supplementary Information (S1, Detailed Methods and Materials).

Plasma reactor design and 3D printing

A flow-through plasma system was employed for the synthesis of multi-metallic NCs. The CAPP system (**Figure 1**) comprised two main components: the lid (**Figure 1**, element 2) and the bottom part (**Figure 1**, element 3). The reactor was designed and fabricated using SLA 3D printing technology. SLA utilises a liquid photopolymer resin that is selectively cured by a laser beam reflected from a mirror. The reactor was printed using a Formlabs Form 3 (MD, USA) with an XY resolution of 25 µm, a laser spot size of 85 µm, a laser power of 250 mW and a laser wavelength of 405 nm. Formlabs *Clear V4* resin was used for the reactor body (**Figure 1**, element 3), while Formlabs *High Temp* resin was employed for the lid (**Figure 1**, element 2). A tungsten electrode with an outer diameter of 3.0 mm was positioned within the lid to serve as the plasma discharge electrode. Technical presentation of the applied CAPP system is provided in **Figure S1** (Supplementary Materials).

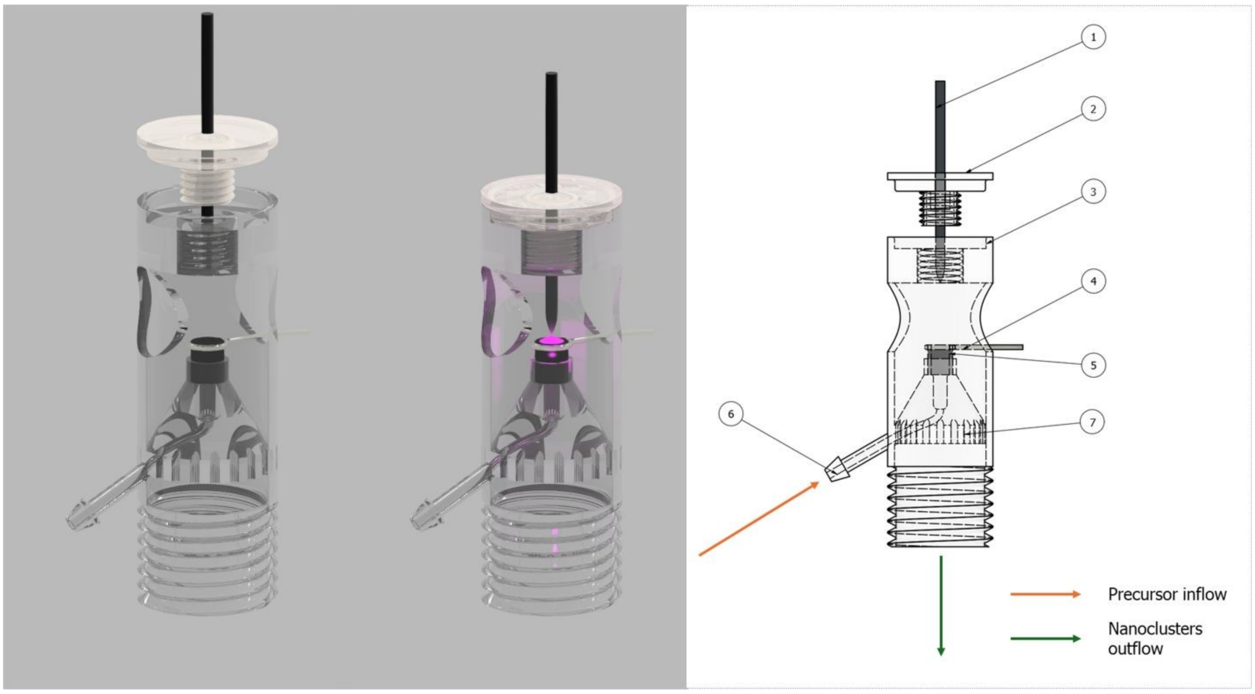

Figure 1. Schematic of the CAPP system: (1) tungsten electrode, (2) lid, (3) bottom part, (4) platinum wire, (5) graphite electrode, (6) inflow port and (7) channel outflows for post-plasma sample collection.

The reactor design, which involved the separate fabrication of the lid, was motivated by the need to mitigate heating of the tungsten electrode. Additional design features, such as threaded components, enabled precise electrode positioning and secure connection of the reactor to the sample collector. The stub is oriented at a 60° angle, ensuring uniform sample flow and preventing the accumulation of air bubbles in the supply channel. Furthermore, the stub terminates in a cut-off cone, facilitating the attachment of the sample supply hose. The sample supply channel also widens at its terminal point,

View Article Online
DOI: 10.1039/D6CY00150F

increasing the contact between the generated CAPP and the liquid sample, thereby stabilising the plasma discharge. Notably, this reactor design eliminates the need for a quartz tube, which is typically employed as an insulator in plasma-based systems [69–72].

Plasma-mediated synthesis of multi-metallic nanoclusters

The designed system was operated in two discharge configurations, in which the CAPP was generated in contact with the flowing NC precursor solution either as an FLA or FLC configuration. In the FLC-dc-APGD configuration, the tungsten electrode is grounded, while the cathode is connected to the graphite rim electrode through which the NC precursor solution flows (**Figure 1**, element 5). The FLA-dc-APGD configuration operates in the opposite manner. In the discharge zone between the tungsten electrode and the flowing NC precursor solution, CAPP was generated and supplied by a DC power supply (DSC-Electronics, Germany). The NC precursor solutions (see preparation in Supplementary Materials, Section S1.2, Reagents and Solutions) were introduced into the CAPP system using a four-channel peristaltic pump (Masterflex L/S, Core-Palmer, USA) at a flow rate of 4 mL min^{-1}, supplied sequentially in a continuous mode. Following plasma treatment, the CAPP-treated solutions containing the formed NCs were promptly collected in glass vials for further characterisation and catalytic experiments. This approach enabled the formation of a series of catalysts comprising a dominant metal and accompanying metals, resulting from the continuous operation of the CAPP system. In this study, the notation used lists the dominant metal first, while accompanying metals are indicated in superscript. The applied current–voltage parameters for the synthesis of multi-metallic NCs are presented in Table S1 (Supplementary Information).

This work provides a comprehensive examination of the synthesis and catalytic performance of a series of catalysts based on metal NCs synthesised from selected transition metals such as Pt, Os, Ru, W and Re, with the addition of Pd and Cr. The selection of the synthesised NCs was not arbitrary; the NCs included in this study were chosen based on their catalytic activity among all metals investigated. Specifically, NCs containing Ir, Pd and Rh as the primary metals were also examined. However, the catalytic performance of these additional NCs was significantly inferior, and therefore, they are not included in the present study, although the corresponding data are available in the dataset at https://doi.org/10.18150/JCA2TE.

Results and discussion

Characteristics of nanoclusters

It was hypothesised that CAPP treatment of NC precursors could influence the morphology and stability of the resulting NCs, thereby affecting their catalytic properties. Accordingly, comprehensive characterisation was performed, including analysis of the particle size distribution by number, polydispersity index (PdI), hydrodynamic diameter (D_h) by intensity, zeta potential (ξ), electrical conductivity (σ) and UV/Vis spectroscopy, in addition to high-resolution transmission electron microscopy (HRTEM). These analyses were carried out for Pt^{Os}NCs, Os$^{Pd/Cr}$NCs, Ru^{W}NCs, W$^{Ru/Os}$NCs and Re^{Os}NCs synthesised using FLA-dc-APGD and/or FLC-dc-APGD. A detailed discussion on these characterisation results is provided in the Supplementary Information (S2.1, NCs characteristic). The UV/Vis spectra are present in **Figure S2**, while the PdI and D_h results are summarised in Table S2.

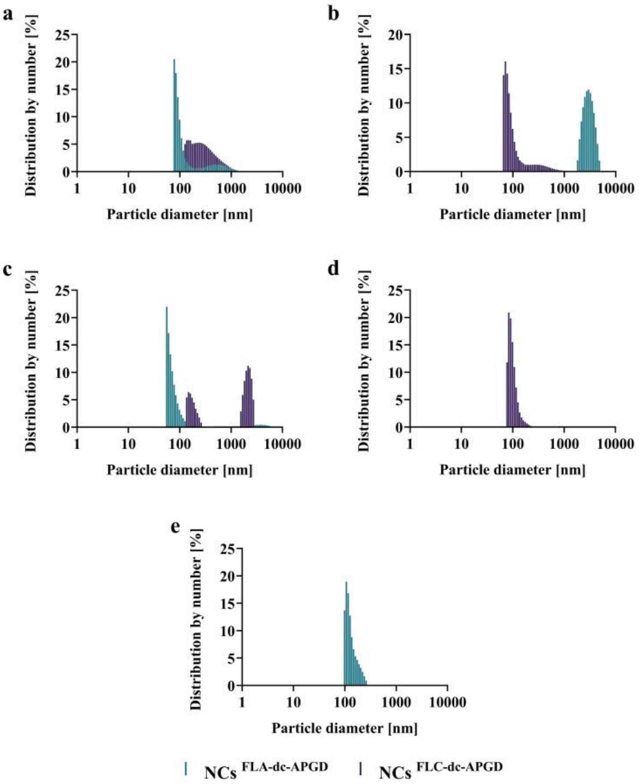

Figure 2. Particle size distributions by number of NCs synthesised by FLA-dc-APGD and FLC-dc-APGD: Pt^{Os}NCs (a), Os$^{Pd/Cr}$NCs (b), Ru^{W}NCs (c), W$^{Ru/Os}$NCs (d) and Re^{Os}NCs (e).

Table 1. Zeta potential (ξ) and conductivity (σ) of NCs synthesised by FLA-dc-APGD and FLC-dc-APGD.

	NCs synthesised by FLA-dc-APGD		NCs synthesised by FLC-dc-APGD	
Sample	ξ [mv]	σ [mS cm^{-1}]	ξ [mv]	σ [mS cm^{-1}]
Pt^{Os}NCs	−8.20 ± 0.97	4.42 ± 0.03	−11.09 ± 2.43	3.36 ± 0.04
Os$^{Pd/Cr}$NCs	9.31 ± 0.23	8.39 ± 0.17	−3.63 ± 0.36	7.69 ± 0.06
Ru^{W}NCs	32.58 ± 0.16	1.16 ± 0.00	32.42 ± 0.46	1.28 ± 0.01
W$^{Ru/Os}$NCs	-*	-*	−38.05 ± 1.23	1.60 ± 0.03
Re^{Os}NCs	−45.59 ± 0.45	1.49 ± 0.02	-*	-*

*The plasma was unstable; therefore, the synthesis was not conducted.

View Article Online
DOI: 10.1039/D6CY00150E

To assess the morphology of the synthesised Pt^{Os}NCs, Os$^{Pd/Cr}$NCs, Ru^{W}NCs, W$^{Ru/Os}$NCs and Re^{Os}NCs produced by dc-APGD, HRTEM was performed. This analysis was further motivated by the expectation that the NCs were significantly smaller than the sizes estimated from dynamic light scattering (DLS) measurements (**Figure 2**). This assumption is supported by previous studies reporting that transition-metal NCs tend to form ultrasmall nanoscale structures [73–78]. Nanometric particles were observed for samples synthesised using both FLA-dc-APGD and FLC-dc-APGD configurations, as shown in **Figures 3** and **4**. Furthermore, plasma generates a space-charge sheath near the catalytic surface, inducing repulsive Coulombic forces between similarly charged particles, which enhances dispersion and produces smaller, more uniform nanoparticles [79]. This is further confirmed by the quantitative analysis of HRTEM photomicrographs, presented as size distribution histograms in **Figure S3** (Supplementary Materials). The HRTEM micrographs reveal the presence of crystallographic planes in Pt^{Os}NCs, Os$^{Pd/Cr}$NCs, Ru^{W}NCs, W$^{Ru/Os}$NCs and Re^{Os}NCs synthesised using CAPP. The particles were predominantly clustered, with structures comprising both agglomerates of atoms and individual atoms in their vicinity. The initial stages of crystalline network formation, resembling the onset of NP organisation, can also be discerned. Consequently, these structures should not be classified as NPs but rather as nanoclusters. The synthesised NCs can be regarded as dynamic systems, as consecutive micrographs acquired from the same region exhibited noticeable temporal variations, indicative of structural mobility. The stability of obtained NCs was evaluated using ξ, with the highest values observed for both dc-APGD synthesised Ru^{W}NCs, for W$^{Ru/Os}$NCs and Re^{Os}NCs (**Table 1**), suggesting their good stability [80]. A detailed discussion is presented in section S2.1 NCs characteristic (see Supplementary Materials). **Figures 3** and **4** also present the corresponding energy-dispersive X-ray (EDX) spectra of the synthesised NCs. The EDX spectra of Pt^{Os}NCs showed peaks corresponding to metallic Pt samples synthesised using both FLA-dc-APGD and FLC-dc-APGD. For Os$^{Pd/Cr}$NCs, metallic Os and Pd were detected in samples produced by FLA-dc-APGD, whereas only metallic Os was observed when the FLC-dc-APGD configuration was employed. Ru^{W}NCs exhibited the presence of Ru under both CAPP configurations. In the case of W$^{Ru/Os}$NCs synthesised by FLC-dc-APGD, EDX analysis indicated the presence of W at the surface. Similarly, EDX spectra of Re^{Os}NCs synthesised using FLA-dc-APGD also revealed the presence of W. Additionally, **Figure S4** (Supplementary Information) presents a comparison of EDX spectra obtained from different regions of the photomicrographs for each of the analysed NCs samples. Based on these results the apparent discrepancies between the EDX results and the expected NCs compositions was observed. These arise from the surface-sensitive nature of EDX analysis, that further experienced challenges related to the imaging of extremely small structures. Because of this, the actual elemental compositions of NC catalysts were determined using inductively coupled plasma optical emission spectroscopy (ICP-OES, **Table S3**), and X-ray photoelectron spectroscopy (XPS) discussed further in this manuscript.

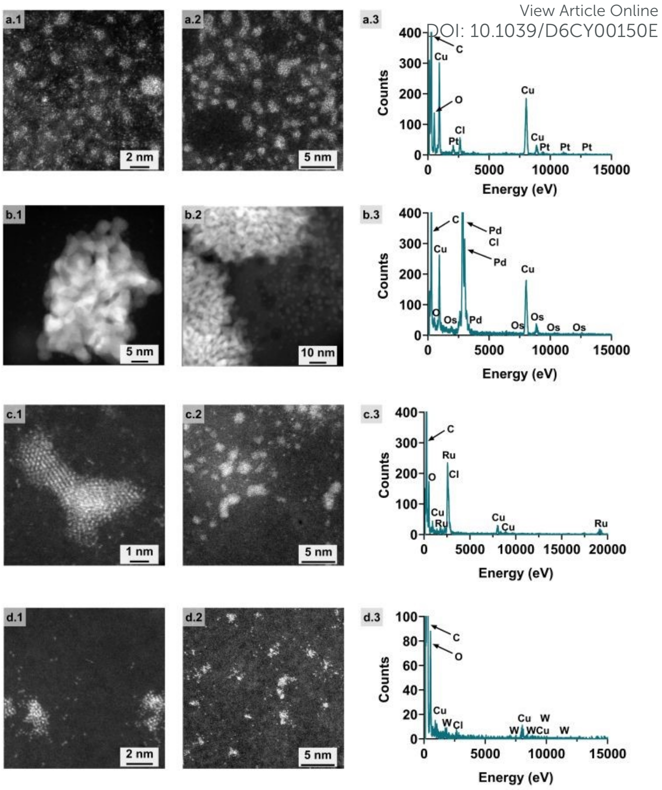

Figure 3. Representative HRTEM photomicrographs (1,2) and EDX spectra (3) of NCs synthesised by FLA-dc-APGD: Pt^{Os}NCs (a), Os$^{Pd/Cr}$NCs (b), Ru^{W}NCs (c) and Re^{Os}NCs (d). Each panel presents pairs of photomicrographs acquired from different perspectives of the same sample.

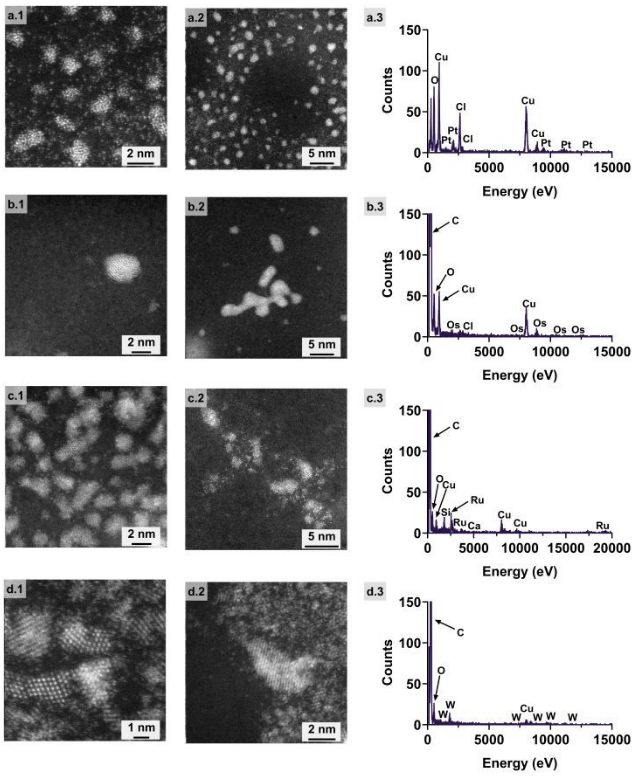

Figure 4. Representative HRTEM photomicrographs (1,2) and EDX spectra (3) of NCs synthesised by FLC-dc-APGD: Pt^{Os}NCs (a), $Os^{Pd/Cr}$NCs (b), Ru^{W}NCs (c) and $W^{Ru/Os}$NCs (d). Each panel presents pairs of photomicrographs acquired from different perspectives of the same sample.

Catalytic activity

Pt^{Os}NCs, $Os^{Pd/Cr}$NCs, Ru^{W}NCs, $W^{Ru/Os}$NCs and Re^{Os}NCs were employed as catalysts for the reduction of 4-NP to 4-aminophenol (4-AP). Their catalytic performance was evaluated by UV/Vis spectrophotometric analysis. The experimental results are presented in **Figure 5**, which illustrates the evolution of the UV/Vis absorption spectra during the 4-NP reduction reaction, and in Table 2, which summarises the corresponding rate constants and 4-NP conversion efficiencies. The data related to the selection of the applied NCs volume are summarised in section S2.2 Catalytic reaction and presented in **Figure S5** (Supplementary Materials).

The initial absorption band at 318 nm is attributed to 4-NP. Following the addition of $NaBH_4$, 4-NP was converted to 4-nitrophenolate ions, resulting in a bathochromic shift of the absorption peak to 400 nm (**Figure 5**) [53]. This peak remained stable until the introduction of the NCs, after which it gradually decreased in intensity, accompanied by the appearance of a new absorption band indicative of 4-AP formation [81]. The latter was observed at approximately 295 nm for Pt^{Os}NCs, ~282 nm for $Os^{Pd/Cr}$NCs, ~310 nm for Ru^{W}NCs, ~300 nm for $W^{Ru/Os}$NCs and Re^{Os}NCs [66].

Although several samples exhibited strong catalytic activity, others were markedly less effective in promoting 4-NP reduction. The mass-normalised rate constant ($k_{1m}{}^{b}$), determined for the 4-NP reduction reaction (Table 2), was highest for Ru^{W}NCs synthesised using FLA-dc-APGD (17.81 min^{-1} mg^{-1}) and FLC-dc-APGD (18.09 min^{-1} mg^{-1}). A comparably high $k_{1m}{}^{b}$ value of 15.87 min^{-1} mg^{-1} was obtained for $Os^{Pd/Cr}$NCs synthesised using the FLA-dc-APGD configuration. These values exceeded those measured for other dc-APGD-synthesised NCs (Table 2). Based on the data presented in **Figure 5** and Table 2, $Os^{Pd/Cr}$NCs synthesised using the FLA-dc-APGD configuration exhibited the highest overall catalytic efficiency. Notably, this catalyst achieved 86% conversion of 4-NP within 1.2 min, whereas all other samples required 8 min to reach their reported conversion levels. In contrast, the lowest catalytic activities were observed for Pt^{Os}NCs and $W^{Ru/Os}$NCs synthesised using FLC-dc-APGD, with $k_{1m}{}^{b}$ values of 0.55 min^{-1} mg^{-1} and 0.50 min^{-1} mg^{-1}, corresponding to 4-NP conversions of 36% and 32%, respectively. For comparison, $k_{1m}{}^{b}$ values were also determined for monometallic OsNCs and RuNCs synthesised using FLA-dc-APGD. The corresponding rate constants were 0.75 min^{-1} mg^{-1} for OsNCs (700 ppm precursor; synthesis parameters: 70 mA, 1250 V, 4 mL min^{-1}) and 14.99 min^{-1} mg^{-1} for RuNCs (600 ppm precursor; synthesis parameters: 52 mA, 1310 V, 5 mL min^{-1}). A detailed discussion of the turnover frequency (TOF) analysis is provided in the Supplementary Information (S2.2, Catalytic reaction), with the corresponding TOF results presented in **Figure S6**.

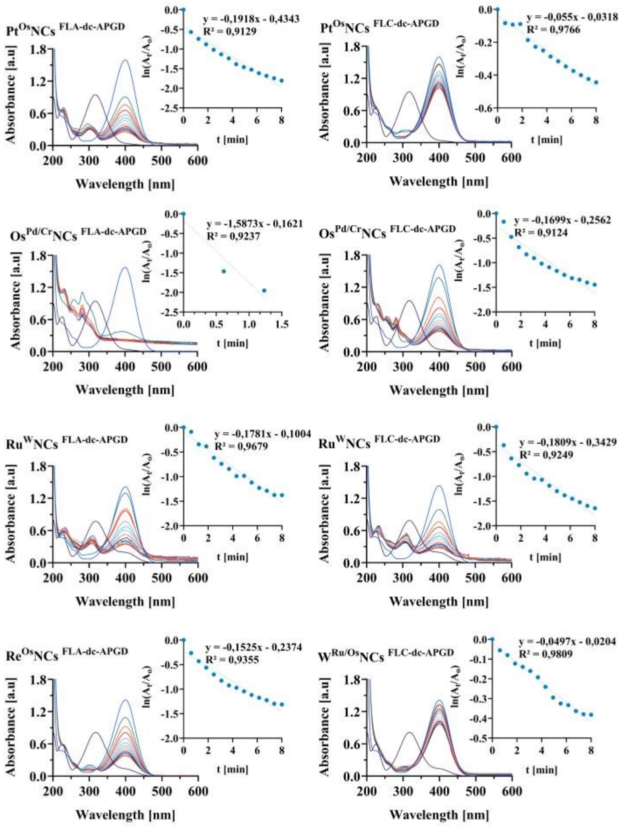

Figure 5. UV/Vis absorption spectra and first-order kinetic plots for the reduction of 4-NP using NCs synthesised by FLA-dc-APGD and FLC-dc-APGD.

View Article Online
DOI: 10.1039/D6CY00150E

Table 2. Overview of the catalytic activity of NCs synthesised using FLC-dc-APGD and FLA-dc-APGD.

	NCs synthesised by FLA-dc-APGD					NCs synthesised by FLC-dc-APGD				
Sample	**t (min)**	**k_1^b (min^{-1})**	**k_{1m}^b (min^{-1} mg^{-1})**	**R^2**	**E (%)**	**t (min)**	**k_1^b (min^{-1})**	**k_{1m}^b (min^{-1} mg^{-1})**	**R^2**	**E (%)**
Pt^{Os}NCs	8.0	0.19	1.92	0.91	84	8.0	0.05	0.55	0.98	36
$Os^{Pd/Cr}$NCs	1.2	1.59	15.87	0.92	86	8.0	0.17	1.70	0.91	76
Ru^{W}NCs	8.0	0.18	17.81	0.97	75	8.0	0.18	18.09	0.92	81
$W^{Ru/Os}$NCs	-*	-*	-*	-*	-*	8.0	0.05	0.50	0.98	32
Re^{Os}NCs	8.0	0.15	1.53	0.94	73	-*	-*	-*	-*	-*

*The plasma was unstable; therefore, the synthesis was not performed.

t denotes the time taken for the corresponding reduction

k_1^b denotes the pseudo-first-order rate constant

k_{1m}^b denotes the mass-normalised rate constant

R^2 denotes the correlation coefficient

E denotes the 4-NP reduction rate (%)

Oxidation states of d-block elements in NCs

X-ray photoelectron spectroscopy (XPS) was employed to determine the oxidation states of Pt, Os, Ru, W and Re, as well as the additional presence of Pd and Cr, in the synthesised NCs. The surface concentrations of chemical species, obtained by fitting the XPS spectra, are summarised in Tables S4–S8 (see Supplementary Information) for all analysed samples.

For Pt^{Os}NCs synthesised using both FLA- and FLC-dc-APGD configurations, the Pt 4f spectra shown in **Figure 6(a,b)** were fitted using a doublet structure ($f_{7/2}$–$f_{5/2}$ splitting of 3.33 eV), with the main $4f_{7/2}$ component centred at 73.4 eV. This binding energy is indicative of the presence of Pt^{2+} species, such as PtO and/or $PtCl_2$ [82–84]. Notably, additional metallic species were detected in both samples. In the FLA-dc-APGD-synthesised Pt^{Os}NCs, signals corresponding to Cr, Pd and W were observed, whereas in the FLC-dc-APGD-synthesised sample, only Cr was detected. Consequently, overlapping contributions from the Cr 3s and W 5s core levels were included in the fitting of the Pt 4f spectra. High-resolution spectra recorded in the regions corresponding to the principal photoelectron lines of Pt^{Os}NCs are provided in the Supplementary Information (**Figure S7**). For $Os^{Pd/Cr}$NCs synthesised using both discharge configurations, the Os 4f spectra (**Figure 6(c,d)**) were fitted with a doublet structure ($f_{7/2}$–$f_{5/2}$ splitting of 2.8 eV), in which the $4f_{7/2}$ peak was centred at 53.6 eV. This binding energy corresponds to either Os^{4+} in OsO_2 and/or Os^{3+} in $OsCl_3$ [85]. Similar to the Pt^{Os}NCs, additional metallic species were detected in $Os^{Pd/Cr}$NCs, with Re and Pd signals observed for samples synthesised using both FLA- and FLC-dc-APGD. The corresponding high-resolution spectra for these elements are presented in the Supplementary Information (**Figure S7**). For Ru^{W}NCs synthesised using both FLA-dc-APGD and FLC-dc-APGD, the Ru $3p_{3/2}$ spectra shown in **Figure 6(e,f)** were fitted with two components. The first component, centred at 463.8 eV, is attributed to Ru^{4+} species, such as RuO_2 and/or Ru^{2+} in $RuCl_2$, while the second component at 465.6 eV originates from the presence of $RuCl_3$ [83,86]. The W 4f spectra (**Figure 6(g,h)**), obtained for Re^{Os}NCs synthesised using FLA-dc-APGD and $W^{Ru/Os}$NCs synthesised using FLC-dc-APGD, were fitted with a doublet structure ($f_{7/2}$–$f_{5/2}$ splitting of 2.18 eV). The main $4f_{7/2}$ peak, centred at 35.5 eV, is indicative of W^{6+} species, such as WO_3, and/or W^{4+} in WCl_4, which appear at similar binding energies [83,87].

View Article Online
DOI: 10.1039/D6CY00150E

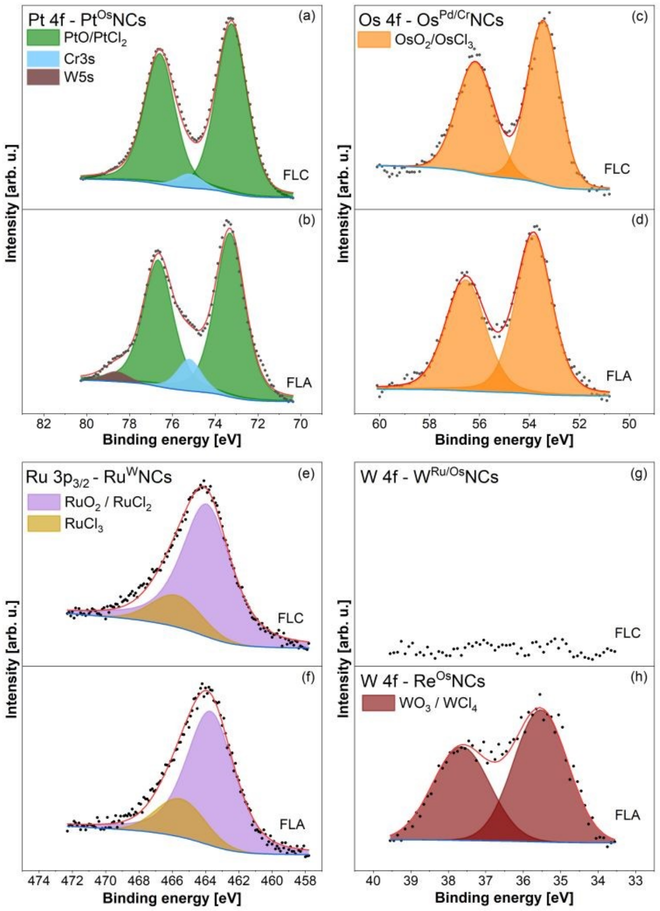

Figure 6. High-resolution XPS spectra of NCs synthesised by FLA- and FLC-dc-APGD: (a,b) Pt 4f, (c,d) Os 4f, (e,f) Ru $3p_{3/2}$ and (g,h) W 4f. Panels (a), (c), (e), and (g) correspond to NCs obtained via FLC-dc-APGD, whereas panels (b), (d), (f), and (h) correspond to those synthesised via FLA-dc-APGD. Spectra were fitted with doublet structures corresponding to the characteristic oxidation states described in the text.

The atomic composition (%) of the NC surfaces is of particular interest and is summarised in Tables S4–S8 (Supplementary Information). As shown in Table S4, the concentration of $PtO/PtCl_2$ in Pt^{Os}NCs synthesised using FLA-dc-APGD is approximately three times lower than that observed for Pt^{Os}NCs synthesised using FLC-dc-APGD. Moreover, the analysis confirms that Pt^{Os}NCs synthesised using FLA-dc-APGD were contaminated with W, Pd and Cr, whereas Pt^{Os}NCs prepared using the FLC-dc-APGD configuration showed contamination only by Cr. $W^{Ru/Os}$NCs and Re^{Os}NCs exhibited W(VI) atomic concentrations of 0.3% and 0.0% for NCs synthesised by FLC-dc-APGD and FLA-dc-APGD, respectively (Tables S7 and S8). These results indicate that the FLC-dc-APGD configuration was less effective in reducing the precursors. A markedly different outcome was observed for $Os^{Pd/Cr}$NCs (Table S5), which displayed atomic concentrations of $OsCl_3/OsO_2$ of 0.60% and 0.43% for FLA-dc-APGD and FLC-dc-APGD syntheses, respectively, with additional Re contamination detected. Similarly, for Ru^WNCs (Table S6), the surface composition of $RuCl_2/RuO_2$ was 7.6% for FLA-dc-APGD and 4.4% for FLC-dc-APGD. The atomic concentrations of $RuCl_3$ were 1.4% and 1.0% for FLA- and FLC-dc-APGD, respectively. These findings indicate that the FLA-dc-APGD configuration is more effective than FLC-dc-APGD in promoting precursor conversion, particularly for $Os^{Pd/Cr}$NCs and Ru^WNCs. These trends in surface composition are consistent with the TOF values and the measured catalytic activities of the nanoclusters.

Plasma induced mechanism of nanocluster synthesis

The obtained and characterized NCs were synthesised using two discharge configurations that differed in their influence on nanostructure formation. In the FLC configuration, the flowing precursor solution surface was irradiated by positive ions [88,89]. Upon reversing the electrode polarity, the discharge operated in FLA mode, in which the surface of the flowing solution is irradiated by the electrons [88,89]. During FLC-dc-APGD treatment the surface of metals from precursor solution is continuously bombarded by positively charged high energy species, e.g. H_2O^+, H_3O^+ ions [53]. Under these conditions, high-energy ions (⊕) were capable of inducing excitation of water molecules, resulting in the subsequent formation of solvated electrons (e_{aq}^-) according to the reaction:

$$\oplus + H_2O \rightarrow H_2O^* \rightarrow H_2O^+ + e_{aq}$$

These solvated electrons could most likely responsible for the reduction of metals present in the analysed NCs. Conversely, low-energy H_2O^+ ions preferentially could underwent recombination reactions with water molecules, leading to the generation of reactive oxygen species, including hydroxyl radicals (•OH) and hydrogen peroxide (H_2O_2) [53,90]:

$$H_2O^+ + H_2O \rightarrow H_3O^+ + OH^\bullet$$

$$OH^\bullet + OH^\bullet \rightarrow H_2O_2$$

In contrast, when FLA-dc-APGD was applied substantial concentration of e_{aq}^- was generated and became available for subsequent reactions within the solution [53]. These electrons can also participated in reduction process. Additionally, recombination reactions between e_{aq}^- and hydronium ions (H_3O^+) could led to the formation of hydrogen radicals (H•), which also exhibit strong reducing properties [53,90–92]:

$$e_{aq} + H_3O^+ \rightarrow H^\bullet + H_2O$$

UV radiation could be observed during dc treatments, therefore the high-energy of UV photons can transfer energy to water molecules, leading to formation or reactive reducing and oxidizing species [91]:

$$H_2O + h\nu \rightarrow H + OH$$

Furthermore, as observed in Table S4 (Supplementary Materials) electron irradiation for the synthesis of Pt^{Os}NCs is more effective than positive ion irradiation, as indicated by the surface compositions of 5.8% and 15.6% for $PtO/PtCl_2$, respectively. This suggest better reduction of $PtCl_6^{2-}$, when using FLA-dc-APGD configuration. In contrast, for $Os^{Pd/Cr}$NCs and Ru^WNCs (Table S5-S6, Supplementary Materials), an opposite effect is observed for both dominant metals, i.e., positive ions irradiation in the plasma is more effective than electron irradiation for the synthesis of these NCs. Additionally, the elevated oxygen signal observed in the EDX spectrum (**Figures 3** and **4**) suggests the presence of oxidized metal forms, which is further corroborated by the XPS results presented in Tables S4–S8 (Supplementary Materials).

View Article Online
DOI: 10.1039/D6CY00150E

Merits of the proposed plasma-assisted synthesis

The successful synthesis of $Pt^{Os}NCs$, $Os^{Pd/Cr}NCs$, $Ru^{W}NCs$, $W^{Ru/Os}NCs$ and $Re^{Os}NCs$ enabled a comprehensive investigation into the catalytic performance of these d-block metal nanoclusters. Particular attention should be paid to secondary sources containing d-block metals. Their utilization may offer considerable economic advantages without compromising catalytic performance, even in the synthesis of multi-metallic catalysts. Based on commercially available reagents, the approximate costs of the catalyst precursors are as follows: Cr < $1, W $2, Re $4, Ru $14, Pd $20, Os $80 and Pt $106. This suggests that secondary sources rich in these metals constitute promising materials that merit further utilization.

The proposed CAPP-based synthesis route represents a quantitatively efficient and environmentally benign approach to the fabrication of multi-metallic NCs. The process operates under ambient pressure and near-room-temperature conditions, without the use of organic solvents, external reducing agents, or high-energy thermal treatments, thereby substantially reducing energy consumption and chemical waste compared to conventional nanocatalyst synthesis methods. The high activity achieved per unit mass of selected multi-metallic NCs (Table 2) indicates improved utilisation of these metals, enabling a reduction in noble metal loading while maintaining or enhancing catalytic efficiency. For this reason, Table 3 presents a comparative analysis of the multi-metallic NCs synthesised in this study with selected d-block metal catalysts reported in the literature. It can be observed that commercially available catalysts exhibit values of rate constants, as well as the normalized rate constants, within the values obtained for our multi-metallic NCs. Notably, $Os^{Pd/Cr}NCs$ demonstrates superior performance, exhibiting both a higher rate constant and a higher mass-normalized rate constant compared to the aforementioned commercial catalysts. It is also worth noting that the use of additively manufactured reactor components supports material-efficient system design and facilitates process scalability, reinforcing the potential of the presented approach as a favourable alternative for catalyst synthesis and application.

Table 3. Comparision of $Pt^{Os}NCs$, $Os^{Pd/Cr}NCs$, $Ru^{W}NCs$, $W^{Ru/Os}NCs$ and $Re^{Os}NCs$ synthesised using FLC-dc-APGD and FLA-dc-APGD with d-block metal-based catalysts.

Catalyst/NPs	Synthesis method	Substrate	k (min^{-1})	k$_m$ (min^{-1} mg^{-1})	Conversion (%)	Reference
ruthenium nanochains	polyol reduction method	4-NP	2.911-25.992	145.55-519.84	99.1-100	[93]
$NiCo_2$	solution phase chemical route	4-NP	0.073	0.073	not provided	[94]
Au-Pd nanoflowers	seed-mediated growth method	4-NP	2.8	555.56	100	[95]
AuNPs	citrate thermal reduction technique	4-NP	0.36	16.67	not provided	[96]
Au-Ag NPs	seed colloidal technique	4-NP	0.52-0.62	not provided	not provided	[96]
Ag/graphene oxide NPs	two-step method	4-NP	0.208	107.22	not provided	[97]
ReNPs	green synthesis	4-NP	0.156-0.162	0.58-0.60	93-99	[98]
Au/CuO and Au/NiO	wet-chemical routes	4-NP	not provided	not provided	100	[99]
Pd/covalent organic frameworks	multi step	4-NP	not provided	not provided	15.3-100	[100]
EnCat Pt^0	commercial catalyst	4-NP	not provided	not provided	15	[101]
Pd/C (5 wt.%)	commercial catalyst	4-NP	0.762	3.048	90	[93]
Ru/C (5 wt.%)	commercial catalyst	4-NP	0.852	3.408	88	[102,103]
Pt, Os, Ru, W, Re, Pd, Cr multi-metallic NCs	CAPP method	4-NP	0.05-1.59	0.50-18.09	<86	this study

k denotes the rate constant

k_m denotes the mass-normalised rate constant

View Article Online
DOI: 10.1039/D6CY00150E

Conclusions

The use of CAPP for NC synthesis allows for the customisation of the experimental setup, which in this work was further enhanced through 3D printing to design and fabricate a reactor tailored to the specific requirements of this study. The results indicate that DLS measurements revealed some particle aggregation in the produced NCs, whereas HRTEM enabled more precise characterisation, confirming particle sizes below 10 nm. The most uniform size distribution, 16.3%, was observed for $Os^{Pd/Cr}$NCs synthesised via FLA-dc-APGD. Enhanced colloidal stability was noted for Ru^{W}NCs prepared using FLA-dc-APGD and FLC-dc-APGD, with zeta potentials of 32.58 ± 0.16 mV and 32.42 ± 0.46 mV, respectively. The optical properties of NCs were similar following both FLA-dc-APGD and FLC-dc-APGD treatments, as evidenced by the UV/Vis spectra. Catalytic activity measurements showed substantially improved 4-NP reduction for Ru^{W}NCs synthesised via FLA-dc-APGD and FLC-dc-APGD, with mass-normalised rate constants of $17.81\ \text{min}^{-1}\ \text{mg}^{-1}$ and $18.09\ \text{min}^{-1}\ \text{mg}^{-1}$, respectively. $Os^{Pd/Cr}$NCs synthesised via FLA-dc-APGD also exhibited high catalytic activity, with a mass-normalised rate constant of $15.87\ \text{min}^{-1}\ \text{mg}^{-1}$. The calculated TOF values are consistent with these catalytic measurements, with the highest TOF values observed for $Os^{Pd/Cr}$NCs ($0.76\ \text{min}^{-1}$ for 20%) and Ru^{W}NCs ($0.89\ \text{min}^{-1}$ for 20%) synthesised using FLA-dc-APGD. This correlation is particularly pronounced for the FLA-dc-APGD configuration, further confirming its superior catalytic performance. Moreover, the surface compositions of $RuCl_2/RuO_2$, $RuCl_3$ and $OsCl_3/OsO_2$ were higher in NCs synthesised via FLA-dc-APGD compared to those prepared using FLC-dc-APGD.

The dc-APGD source employed in this study has proven effective for NC synthesis. Considering the catalytic activity of Pt^{Os}NCs, $Os^{Pd/Cr}$NCs, Ru^{W}NCs, $W^{Ru/Os}$NCs and Re^{Os}N, multi-metallic NCs were analysed in this study to simulate materials that could potentially be produced from metals recovered from secondary sources, which makes their synthesis fully justified. Overall, the FLA discharge configuration favours the production of NCs with superior catalytic activity, with $Os^{Pd/Cr}$NCs and Ru^{W}NCs synthesised via FLA-dc-APGD showing the most promising performance. The use of stabilisers to prevent uncontrolled growth, aggregation and sedimentation of NCs could be explored in future studies to further enhance stability and performance.

CRediT authorship contribution statement

Angelika Nowak: Writing–original draft, Writing–review & editing, Visualisation, Validation, Methodology, Investigation, Formal analysis, Data Curation, Conceptualisation. **Piotr Jamroz:** Supervision, Writing–review & editing, Investigation, Conceptualisation. **Mateusz M. Marzec, Andrzej Bernasik:** Writing–review & editing, Methodology, Investigation. **Krystian Sokolowski:** Investigation. **Anna Dzimitrowicz:** Validation, Writing–review & editing. **Paweł Pohl:** Investigation, Validation, Writing–review & editing. **Piotr Cyganowski**: Supervision, Writing–review & editing, Resources, Project administration, Methodology, Investigation, Funding acquisition, Conceptualisation.

Conflicts of interest

The authors declare no competing financial or personal interests that could have influenced the results of this work.

Data availability statement

All data associated with the synthesis and evaluation of the catalysts presented in this study are available under the permanent identifier: https://doi.org/10.18150/SSL3GB. The results presented in this paper are a part of wider research covering synthesis and evaluation of catalytic activity of selected d-block elements. This covers the research on multimetallic nanocluster catalysts based on Ir, Rh and Pd. The data related to these results are available under the identifier: https://doi.org/10.18150/JCA2TE

Acknowledgments

This research was co-financed by the National Science Centre (NCN, Poland) under the OPUS 25 project (2023/49/B/ST8/01029), awarded to P. Cyganowski. For the purposes of Open Access, the author has applied a CC-BY public copyright licence to any Author Accepted Manuscript version arising from this submission. Graphical abstract was created using BioRender.com under the licence of Wroclaw University of Science and Technology, Poland (https://BioRender.com/qasim2r). Technical documentation forming a part of **Figure 1** was created in Autodesk Inventor Professional 2025 under the licence granted to Wroclaw University of Science and Technology.

Declaration of generative AI and AI-assisted technologies in the writing process:

AI-assisted language refinement using ChatGPT (GPT-5) was applied solely to improve grammatical accuracy and clarity of the text.

References

1 G. Liu, M. J. Arellano-Jiménez, C. B. Carter and A. G. Agrios, *Journal of Nanoparticle Research*, 2013, **15**, 1–13.
2 Y. Guo, M. Wang, Q. Zhu, D. Xiao and D. Ma, *Nat. Catal.*, 2022, **5**, 766–776.
3 D. Astruc, *Chem. Rev.*, 2020, **120**, 461–463.
4 T. Imaoka, H. Kitazawa, W. J. Chun and K. Yamamoto, *Angew. Chem. Int. Ed.*, 2015, **54**, 9810–9815.

View Article Online
DOI: 10.1039/D6CY00150E

5 Q. Tang, G. Hu, V. Fung and D. E. Jiang, *Acc. Chem. Res.*, 2018, **51**, 2793–2802.
6 L. Liu and A. Corma, *Chem. Rev.*, 2018, **118**, 4981–5079.
7 K. Bloch, K. Pardesi, C. Satriano and S. Ghosh, *Front. Chem.*, 2021, **9**, 624344.
8 N. Joudeh, A. Saragliadis, G. Koster, P. Mikheenko and D. Linke, *Frontiers in Nanotechnology*, 2022, **4**, 1062608.
9 A. Ishikawa, T. Doi and H. Nakai, *J. Catal.*, 2018, **357**, 213–222.
10 B. Lin, K. Wei, J. Lin and J. Ni, *Catal. Commun.*, 2013, **39**, 14–19.
11 G. S. Fonseca, G. Machado, S. R. Teixeira, G. H. Fecher, J. Morais, M. C. M. Alves and J. Dupont, *J. Colloid Interface Sci.*, 2006, **301**, 193–204.
12 H. Jeong, G. Lee, B. S. Kim, J. Bae, J. W. Han and H. Lee, *J. Am. Chem. Soc.*, 2018, **140**, 9558–9565.
13 S. Anantharaj, K. Sakthikumar, A. Elangovan, G. Ravi, T. Karthik and S. Kundu, *J. Colloid Interface Sci.*, 2016, **483**, 360–373.
14 J. Luo and C. Liang, *ACS Catalysis* , 2024, **14**, 7032–7049.
15 J. P. C. Coverdale, C. Sanchez-Cano, G. J. Clarkson, R. Soni, M. Wills and P. J. Sadler, *Chemistry – A European Journal*, 2015, **21**, 8043–8046.
16 X. Zhao, Y. Chang, W. J. Chen, Q. Wu, X. Pan, K. Chen and B. Weng, *ACS Omega*, 2021, **7**, 17–31.
17 K. M. Minachev, V. I. Avaev and M. A. Ryashentseva, *Bulletin of the Academy of Sciences of the USSR Division of Chemical Science*, 1986, **35**, 280–283.
18 P. Veerakumar, R. Madhu, S. M. Chen, V. Veeramani, C. Te Hung, P. H. Tang, C. Bin Wang and S. Bin Liu, *J. Mater. Chem. A Mater.*, 2014, **2**, 16015–16022.
19 S. Muthusamy, N. Kumarswamyreddy, V. Kesavan and S. Chandrasekaran, *Tetrahedron Lett.*, 2016, **57**, 5551–5559.
20 W. L. Dai, J. Ding, Q. Zhu, R. Gao and X. Yang, *Catalysis*, 2016, **28**, 1–27.
21 Y. Li, Y. Fan, J. Jian, L. Yu, G. Cheng, J. Zhou and M. Sun, *Catal. Today*, 2017, **281**, 542–548.
22 P. Veerakumar, C. Rajkumar, S. M. Chen, B. Thirumalraj and K. C. Lin, *Electrochim. Acta*, 2018, **271**, 433–447.
23 M. Rafique, Q. Fu, J. Han, R. Wang, T. Yao, X. Wang and B. Song, *ChemElectroChem*, 2024, **11**, e202300722.
24 L. A. MacAdams, G. P. Buffone, C. D. Incarvito, A. L. Rheingold and K. H. Theopold, *J. Am. Chem. Soc.*, 2005, **127**, 1082–1083.
25 K. H. Theopold, *Eur. J. Inorg. Chem.*, 1998, **1**, 15–24.
26 E. Antolini, *J. Mater. Sci.*, 2003, **38**, 2995–3005.
27 Z. Yin, L. Lin and D. Ma, *Catal. Sci. Technol.*, 2014, **4**, 4116–4128.
28 M. V. Twigg, *Transactions of the Institutions of Mining and Metallurgy, Section B: Applied Earth Science*, 2005, **114**, 158–172.
29 K. M. Adams and H. S. Gandhi, *Industrial and Engineering Chemistry Product Research and Development*, 2002, **22**, 207–212.
30 N. Palaniyandy, S. Kutloano, L. Devaraj, X. Fuku and S. S. Dhilip Kumar, *Current Research in Green and Sustainable Chemistry*, 2025, **10**, 100446.
31 H. U. Blaser, A. Indolese, A. Schnyder, H. Steiner and M. Studer, *J. Mol. Catal. A Chem.*, 2001, **173**, 3–18.
32 G. Chelucci, S. Baldino and W. Baratta, *Acc. Chem. Res.*, 2015, **48**, 363–379.
33 G. Anello, G. De Luna, G. De Felice, A. Saker, L. Di Felice and F. Gallucci, *Int. J. Hydrogen Energy*, 2024, **86**, 922–930.
34 P. Veerakumar, S. T. Hung, P. Q. Hung and K. C. Lin, *J. Agric. Food Chem.*, 2022, **70**, 8523–8550.
35 Y. Huang, Y. Ma, Y. Cheng, L. Wang and X. Li, *Appl. Catal. A Gen.*, 2015, **495**, 124–130.
36 P. Veerakumar, N. Dhenadhayalan, K. C. Lin and S. Bin Liu, *J. Mater. Chem. A Mater.*, 2015, **3**, 23448–23457.
37 P. Veerakumar, R. Pandiyan, S. M. Chen, P. Thanasekaran and K. Saranya, *Coord. Chem. Rev.*, 2025, **527**, 216382.
38 Y. Y. Chong, W. Y. Chow and W. Y. Fan, *J. Colloid Interface Sci.*, 2012, **369**, 164–169.
39 M. S. Z. Shiri, W. Henderson and M. R. Mucalo, *Materials*, 2019, **12**, 1896.
40 T. Wang, R. Hu, H. Wei, Z. Wei, M. Luo and Y. Yang, *Nano Energy*, 2025, **133**, 110468.
41 M. Santhosh Kumar, N. Hammer, M. Rønning, A. Holmen, D. Chen, J. C. Walmsley and G. Øye, *J. Catal.*, 2009, **261**, 116–128.
42 J. L. Cao, Y. Wang, T. Y. Zhang, S. H. Wu and Z. Y. Yuan, *Appl. Catal. B*, 2008, **78**, 120–128.
43 N. Karousis, N. Tagmatarchis and D. Tasis, *Chem. Rev.*, 2010, **110**, 5366–5397.
44 C. Queffélec, M. Petit, P. Janvier, D. A. Knight and B. Bujoli, *Chem. Rev.*, 2012, **112**, 3777–3807.
45 M. Kusche, K. Bustillo, F. Agel and P. Wasserscheid, *ChemCatChem*, 2015, **7**, 766–775.
46 Z. Sun, B. Sun, M. Qiao, J. Wei, Q. Yue, C. Wang, Y. Deng, S. Kaliaguine and D. Zhao, *J. Am. Chem. Soc.*, 2012, **134**, 17653–17660.
47 T. Zhang, S. Weng, X. Wang, Z. Zhang, Y. Gao, T. Lin, Y. Zhu, W. Zhang and C. Sun, *J. Colloid Interface Sci.*, 2022, **624**, 704–712.
48 Q. Tian, L. Bi, S. Lin, J. Gao and Y. He, *Clean Energy Science and Technology*, 2024, **2**, 131–131.
49 B. Xv, Z. Li, G. Zha, D. Liu, B. Yang and W. Jiang, *Resour. Conserv. Recycl.*, 2025, **215**, 108103.
50 L. Shen, F. Tesfaye, X. Li, D. Lindberg and P. Taskinen, *Miner. Eng.*, 2021, **161**, 106719.
51 T. N. Angelidis, D. Rosopoulou and V. Tzitzios, *Ind. Eng. Chem. Res.*, 1999, **38**, 1830–1836.
52 A. Nobahar, J. D. Carlier and M. C. Costa, *Clean Technol. Environ. Policy*, 2023, **25**, 2707–2726.
53 P. Cyganowski, D. Terefinko, P. Jamroz, P. Pohl and A. Dzimitrowicz, *RSC Adv.*, 2021, **11**, 38596–38604.
54 X. Xu, D. Ma, P. Zheng, H. Yang, J. Hu, Y. Luo and C. Lai, *J. Mater. Chem. A Mater.*, 2026.
55 M. Cui, F. Wang, W. Zhao, D. Zhang, R. Liang, Q. Ou and S. Zhang, *Chemical Engineering Journal*, 2023, **460**, 141676.
56 J. Shim, K. Y. Joung, J. H. Ahn and W. M. Lee, *J. Electrochem. Soc.*, 2007, **154**, B165.
57 E. S. Gnanakumar, W. Ng, B. Coşkuner Filiz, G. Rothenberg, S. Wang, H. Xu, L. Pastor-Pérez, M. M. Pastor-Blas, A. Sepúlveda-Escribano, N. Yan and N. R. Shiju, *ChemCatChem*, 2017, **9**, 4159–4163.
58 M. Müller, M. Dworschak, J. Benedikt and L. Kienle, *Particle & Particle Systems Characterization*, 2024, **41**, 2400037.
59 F. Yang, Y. Li, T. Liu, K. Xu, L. Zhang, C. Xu and J. Gao, *Chemical Engineering Journal*, 2013, **226**, 52–58.
60 A. Dittmar and D. Herein, *Surf. Coat. Technol.*, 2009, **203**, 992–997.
61 Z. Jie, W. Wenhua, Z. Tingjiang, B. Panek and H. Kierzkowska-Pawlak, *Plasma Phys. Control. Fusion*, 2025, **67**, 055034.
62 S. Rawat, N. Misra, M. Singh, A. Ghosh, S. A. Shelkar, M. Tiwari, S. Samanta and V. Kumar, *Chemical Engineering Journal*, 2024, **498**, 155271.

View Article Online
DOI: 10.1039/D6CY00150E

63 P. Dong, X. Cheng, Z. Jin, Z. Huang, X. Nie, X. Wang and X. Zhang, *J. Photochem. Photobiol. A Chem.*, 2019, **382**, 111971.

64 P. Cyganowski, D. Terefinko, M. A. Khan, A. Motyka-Pomagruk, M. M. Marzec, S. Arabasz, K. Sokolowski, P. Pohl, A. Bernasik, A. Goleniewska, P. Jamroz and A. Dzimitrowicz, *Sci. Rep.*, 2025, **15**, 41789-.

65 P. Cyganowski, M. Caban, M. A. Khan, M. M. Marzec, A. Zak, P. Pohl, P. Jamroz, A. Bernasik and A. Dzimitrowicz, *Plasma Chemistry and Plasma Processing*, 2022, **43**, 199–224.

66 M. A. Khan, P. Cyganowski, P. Pohl, P. Jamroz, W. Tylus, A. Motyka-Pomagruk and A. Dzimitrowicz, *Colloids Surf. A Physicochem. Eng. Asp.*, 2024, **695**, 134190.

67 A. Dzimitrowicz, P. Cyganowski, P. Pohl, D. Jermakowicz-Bartkowiak, D. Terefinko and P. Jamroz, *Nanomaterials*, 2018, **8**, 619.

68 P. Cyganowski, D. Jermakowicz-Bartkowiak, P. Jamroz, P. Pohl and A. Dzimitrowicz, *Colloids Surf. A Physicochem. Eng. Asp.*, 2019, **582**, 123886.

69 A. Dzimitrowicz, T. Lesniewicz, K. Greda, P. Jamroz, M. Nyk and P. Pohl, *RSC Adv.*, 2015, **5**, 90534–90541.

70 T. Q. X. Le, L. N. Nguyen, T. T. Nguyen, E. H. Choi, Q. L. Nguyen, N. K. Kaushik and N. T. Dao, *Applied Sciences*, 2022, **12**, 10308.

71 N. Mohd Nasir, B. K. Lee, S. S. Yap, K. L. Thong and S. L. Yap, *Arch. Biochem. Biophys.*, 2016, **605**, 76–85.

72 L. T. Q. Xuan, L. N. Nguyen and N. T. Dao, *Nanotechnology*, 2021, **33**, 105603.

73 Y. Hattori, S. Nomura, S. Mukasa, H. Toyota, T. Inoue and T. Kasahara, *J. Alloys Compd.*, 2013, **560**, 105–110.

74 Y. Guo, W. Zhang, Y. Sun and M. Dai, *MethodsX*, 2018, **5**, 795–796.

75 A. Pal, S. Shah, S. Belochapkine, D. Tanner, E. Magner and S. Devi, *Colloids Surf. A Physicochem. Eng. Asp.*, 2009, **337**, 205–207.

76 Z. V. Kaidanovych, Y. Y. Kalishyn and P. E. Strizhak, *Theoretical and Experimental Chemistry*, 2013, **48**, 376–380.

77 A. D. Shafigulina, A. A. Revina, N. P. Platonova, S. A. Borovikova and A. K. Buryak, *Colloid Journal*, 2019, **81**, 292–297.

78 M. Marín-Almazo, J. A. Ascencio, M. Pérez-Álvarez, C. Gutiérrez-Wing and M. José-Yacamán, *Microchemical Journal*, 2005, **81**, 133–138.

79 N. Joshi and S. Loganathan, *Catalysts*, 2024, **14**, 802.

80 R. Dewil, J. Baeyens and B. Caerts, *Nano Today*, 2025, **64**, 102783.

81 P. Veerakumar, P. Thanasekaran, K. C. Lin and S. Bin Liu, *J. Colloid Interface Sci.*, 2017, **506**, 271–282.

82 S. Porsgaard, L. R. Merte, L. K. Ono, F. Behafarid, J. Matos, S. Helveg, M. Salmeron, B. Roldan Cuenya and F. Besenbacher, *ACS Nano*, 2012, **6**, 10743–10749.

83 A. D. Wagner, A. V. Naumkin, A. Kraut-Vass, J. W. Allison, C. J. Powell and J. R. J. Rumble, NIST Standard Reference Database 20, https://srdata.nist.gov/xps/, (accessed 4 November 2025).

84 A. S. Aricò, A. K. Shukla, H. Kim, S. Park, M. Min and V. Antonucci, *Appl. Surf. Sci.*, 2001, **172**, 33–40.

85 D. D. Sarma and C. N. R. Rao, *J. Electron Spectros. Relat. Phenomena*, 1980, **20**, 25–45.

86 D. J. Morgan, *Surface and Interface Analysis*, 2015, **47**, 1072–1079.

87 T. A. Carlson and G. E. McGuire, *J. Electron Spectros. Relat. Phenomena*, 1972, **1**, 161–168.

88 A. Dzimitrowicz, P. Jamroz, M. Nyk and P. Pohl, *Materials*, 2016, **9**, 268.

89 K. Greda, K. Swiderski, P. Jamroz and P. Pohl, *Anal. Chem.*, 2016, **88**, 8812–8820.

90 F. Tochikubo, Y. Shimokawa, N. Shirai and S. Uchida, *Jpn. J. Appl. Phys.*, 2014, **53**, 126201.

91 Q. Chen, J. Li and Y. Li, *J. Phys. D Appl. Phys.*, 2015, **48**, 424005.

92 J. Ma, S. Yamashita, Y. Muroya, Y. Katsumura and M. Mostafavi, *Physical Chemistry Chemical Physics*, 2015, **17**, 22934–22939.

93 P. Veerakumar, A. Sangili, S. M. Chen and N. Karuppusamy, *ACS Appl. Nano Mater.*, 2023, **6**, 19740–19755.

94 K. L. Wu, X. W. Wei, X. M. Zhou, D. H. Wu, X. W. Liu, Y. Ye and Q. Wang, *Journal of Physical Chemistry C*, 2011, **115**, 16268–16274.

95 T. Ma, F. Liang, R. Chen, S. Liu and H. Zhang, *Nanomaterials*, 2017, **7**, 239.

96 N. Berahim, W. J. Basirun, B. F. Leo and M. R. Johan, *Catalysts*, 2018, **8**, 412.

97 T. Wu, L. Zhang, J. Gao, Y. Liu, C. Gao and J. Yan, *J. Mater. Chem. A Mater.*, 2013, **1**, 7384–7390.

98 A. Kuś, A. Leśniewicz, A. Dzimitrowicz, P. Pohl and P. Cyganowski, *Int. J. Mol. Sci.*, 2024, **25**, 11319.

99 M. Gholinejad, R. Khezri, S. Nayeri, R. Vishnuraj and B. Pullithadathil, *Molecular Catalysis*, 2022, **530**, 112601.

100 X. Deng, L. Zhu, H. Zhang, L. Li, N. Zhao, J. Wang, S. M. Osman, R. Luque and B. H. Chen, *Environ. Res.*, 2022, **214**, 114027.

101 C. Ramirez Côté, R. Ciriminna, V. Pandarus, F. Béland and M. Pagliaro, *Org. Process Res. Dev.*, 2018, **22**, 1852–1855.

102 J. Wang, Z. Yuan, R. Nie, Z. Hou and X. Zheng, *Ind. Eng. Chem. Res.*, 2010, **49**, 4664–4669.

103 V. Höller, D. Wegricht, I. Yuranov, L. Kiwi-Minsker and A. Renken, *Chem. Eng. Technol.*, 2000, **23**, 251–255.

View Article Online
DOI: 10.1039/D6CY00150E

Data availability statement

All data associated with the synthesis and evaluation of the catalysts presented in this study are available under the permanent identifier: https://doi.org/10.18150/SSL3GB. The results presented in this paper are a part of wider research covering synthesis and evaluation of catalytic activity of selected d-block elements. This covers the research on multimetallic nanocluster catalysts based on Ir, Rh and Pd. The data related to these results are available under the identifier: https://doi.org/10.18150/JCA2TE.